Research Article Vol. 31, No. 16 / 31 Jul 2023 / Optics Express 26178
Optics EXPRESS

3D-printed high-birefringence THz hollow-core anti-resonant fiber with an elliptical core

LU XUE,[1] XINZHI SHENG,[1] QIYUAN MU,[2] DEPENG KONG,[2] ZHAOJIN WANG,[3] PAUL K. CHU,[4] AND SHUQIN LOU[5,*]

[1]School of Physical Science and Engineering, Beijing Jiaotong University, Beijing, 100044, China
[2]State Key Laboratory of Transient Optics and Photonics, Xi'an Institute of Optics and Precision Mechanics, Chinese Academy of Sciences, Xi'an, 710119, China
[3]School of Physics and Optoelectronics Technology, Baoji University of Arts and Science, Baoji, 721016, China
[4]Department of Physics, Department of Materials Science & Engineering, and Department of Biomedical Engineering, City University of Hong Kong, Tat Chee Avenue, Kowloon, Hong Kong, China
[5]Key Laboratory of Communication and Information Systems, Beijing Municipal Commission of Education, School of Electronic and Information Engineering, Beijing Jiaotong University, Beijing, 100044, China
*shqlou@bjtu.edu.cn

Abstract: A high-birefringence and low-loss terahertz (THz) hollow-core anti-resonant fiber (THz HC-ARF) is designed and analyzed numerically by the finite element method (FEM). The THz HC-ARF is composed of an elliptical tube as the core for high birefringence guidance and a pair of symmetrical slabs arranged vertically as the cladding to attain low loss. Numerical analysis indicates that the birefringence reaches 10^{-2} in the transmission window between 0.21 and 0.35 THz. The highest birefringence is 4.61×10^{-2} at 0.21 THz with a loss of 0.15 cm^{-1}. To verify the theoretical results, the THz HC-ARF is produced by three-dimensional (3D) printing, and the transmission characteristics are determined by THz time-domain spectroscopy (THz-TDS). High birefringence in the range of 2.17×10^{-2} to 3.72×10^{-2} and low loss in the range of 0.12 to 0.18 cm^{-1} are demonstrated experimentally in the 0.2 to 0.27 THz transmission window. The highest birefringence is 3.72×10^{-2} at 0.22 THz and the corresponding loss is 0.18 cm^{-1}. The THz HC-ARF shows the highest birefringence besides relatively low loss compared to similar THz HC-ARFs reported recently.

1. Introduction

Polarization plays an important role in terahertz (THz) devices and applications such as communication [1,2], sensing [3], polarized THz filters [4,5], and THz time-domain spectroscopy [6]. Environmental interferences and fabrication imperfections can produce random birefringence in photonic crystal fibers (PCFs) consequently hampering commercial applications [7,8]. In this respect, polarization-maintaining (PM) THz PCFs can eliminate unpredictable polarization. In the PM THz PCF, modal birefringence introduced by the geometrical asymmetry or internal stress can counteract environmental disturbances thus enabling high light polarization purity over long PCF distances under realistic conditions. Porous-core THz PCFs with high birefringence properties have been studied [5,9–14]. For example, Islam *et al.* [15] have introduced dual-asymmetry to the absorbent-core THz PCF to accomplish high birefringence of 0.045 and low loss of 0.08 cm^{-1} (0.35 dB/cm) at 1 THz. However, in high-birefringence THz PCFs, the porous-core materials and the different β introduce fundamental limitations such as materials absorption, high non-linearity, and polarization mode dispersion, which are difficult to overcome.

Hollow-core THz PCFs with guided light in the air-core can address these fundamental limitations. Two types of hollow-core THz PCFs, namely the hollow-core photonic bandgap fibers (HC-PBGFs) and hollow-core anti-resonant fibers (HC-ARFs), have been studied [16,17].

#497258 https://doi.org/10.1364/OE.497258
Journal © 2023 Received 7 Jun 2023; revised 16 Jul 2023; accepted 17 Jul 2023; published 21 Jul 2023

Optics EXPRESS

HC-PBGFs use the photonic bandgap effect to guide light in the air core [18–20] to obtain birefringence by utilizing the asymmetrical core shape. Xiao *et al*. have reported a quasi-elliptical core THz HC-PBGF with birefringence of 9.4×10^{-4}, confinement loss of 3×10^{-3} cm$^{-1,}$ and group velocity dispersion of 0.39 ps/THz/cm at 0.9 THz [21]. However, because highly birefringent THz HC-PBGFs have some insurmountable drawbacks including the narrow bandwidth, complex structure, and fabrication complexity, the use of THz HC-PBGFs in communication applications and polarized THz filters has been limited.

Fortunately, almost all the aforementioned drawbacks plaguing THz HC-PBGFs can be overcome by another type of THz PCFs, i.e., the THz HC-ARF, also known as the inhibited-coupling hollow-core fiber [22,23] which boasts a wider transmission window, lower loss, and simple fabrication. However, on account of light guidance in the air core and the small overlap between light and materials, it is challenging for THz HC-ARFs to obtain high birefringence ($\sim 10^{-4}$). An elliptical polymer tube with high birefringence on the order of 0.01 has been incorporated into the high-birefringence THz HC-ARF [24], and Vincetti *et al*. have investigated a high-birefringence THz HC-ARF with a cladding composed of circular tubes in elliptical arrangement [25]. However, the birefringence is less than 7×10^{-5}. A THz HC-ARF with two large cladding tubes with birefringence of 7.31×10^{-4} at 1.20 THz has been proposed [26] and Yang *et al*. have fabricated a simple elliptical THz HC-ARF by means of three-dimensional (3D) printing [27]. The birefringence measured experimentally is on the level of 10^{-4}, but the operating bandwidth is narrow. A birefringent THz HC-ARF composed of four semielliptical cladding tubes with different wall thicknesses has been proposed [28]. The birefringence is 1.52×10^{-4} at 0.90 THz and the loss of fundamental mode (FM) is 0.0012 cm^{-1} (0.50 dB/m). Du *et al*. have observed high birefringence up to 10^{-2} by introducing a thin strut microstructure into the THz HC-ARF [29]. However, the high effective material loss is a problem in commercial applications. Recently, our group has developed a high-birefringence THz HC-ARF encompassing two pairs of symmetrical parallel slabs in a circular tube [1]. The highest birefringence measured experimentally is 4.77×10^{-3} at 0.39 THz and the corresponding loss is 0.12 cm^{-1}. In spite of recent advances in THz HC-ARFs, state-of-the-art fabricated birefringent THz HC-ARF show birefringence of only 10^{-3} and hence, the development of high-birefringence and low-loss THz HC-ARFs that can be manufactured by simple processes is crucial to commercial adoption.

Herein, a high-birefringence THz HC-ARF with a low loss is designed, simulated, optimized, and demonstrated experimentally. The THz HC-ARF is composed of an elliptical tube as the core to provide high birefringence guidance and a pair of symmetrical slabs is arranged vertically as the cladding to accomplish low loss. The transmission characteristics are analyzed by the finite-element method (FEM) with the aid of the perfect matching layer (PML). Experimentally, the THz HC-ARF is prepared by 3D printing and analyzed by THz time-domain spectroscopy (THz-TDS) to confirm the predicted high-birefringence and low-loss in the THz regime. The experimental and theoretical results are consistent. The highest birefringence determined experimentally is 3.72×10^{-2} at 0.22 THz and the loss is 0.18 cm^{-1}. This THz HC-ARF shows the highest birefringence and low loss compared to similar THz HC-ARFs reported recently.

2. THz HC-ARF structure and principle

Figure 1 (a) depicts the cross-section of the THz HC-ARF with an elliptical core supported by a bar (Bar-THz HC-ARF). The gray areas represent photosensitive resin commonly used in 3D printing and the white areas are dry air. The average refractive index of photosensitive resin measured on the THz-TDS system is 1.6778 + i 0.045 in the frequency range from 0.2 to 1 THz, which is later introduced in Section 4. As shown in Fig. 1 (a), the Bar-THz HC-ARF is composed of an elliptical tube as the core for high birefringence guidance and a pair of symmetrical slabs arranged vertically as the cladding to minimize loss. The strut thickness, t_1, depicts the thickness of the core and cladding except for the support bar which is labeled as t_2. The major and minor

Optics EXPRESS

axes of the elliptical tube core are a and b, respectively. The distance between the pair of slabs and the core is d and the wall thickness and inner radius of the outer circular tube as a protective layer are represented by h and R, respectively. The suspended elliptical tube THz HC-ARF (S-THz HC-ARF) with $t_2 = 0$ shown in Fig. 1 (b) represents the ideal structure of the Bar-THz HC-ARF. The Bar-THz HC-ARF is the modified version of the S-THz HC-ARF with bar supports to form a realistic structure.

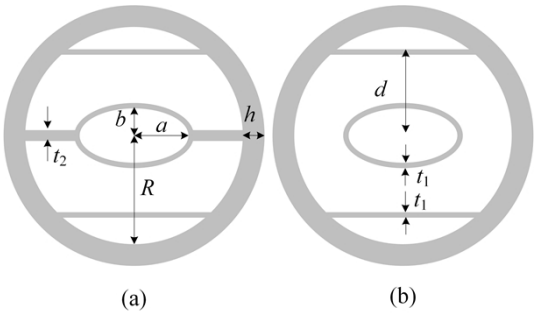

Fig. 1. Cross-sectional of the (a) Bar-THz HC-ARF and (b) S-THz HC-ARF.

The resonant frequencies of a THz HC-ARF are determined by Eq. (1) [30]:

$$f_{\mathrm{m}} = \frac{mc}{2t\sqrt{n^2 - 1}} \tag{1}$$

where c is the speed of light in vacuum, t is the wall thickness of the THz HC-ARF, n is the real part of the material refractive index, and m is an integer. The birefringence B of the THz HC-ARF is expressed as [29]:

$$B = |n_{\mathrm{y}} - n_{\mathrm{x}}|, \tag{2}$$

where n_{x} and n_{y} are the effective refractive indexes of X- and Y- polarized fundamental modes (FMs), respectively. The transmission loss including the effective material loss and confinement loss is calculated by Eq. (3) [1]:

$$\mathrm{Loss} = k_0 \mathrm{Im}(\tilde{n}). \tag{3}$$

where k_0 is the wave vector in the vacuum and $\mathrm{Im}(\tilde{n})$ is the imaginary part of the complex refractive index.

To investigate the birefringence and loss of the THz HC-ARF, the finite element method (FEM) based on the software COMSOL Multiphysics with the perfect matching layer (PML) is utilized to analyze the characteristics of the THz HC-ARF. To simplify the complexity in optimizing the design, a THz HC-ARF without support bars (S-THz HC-ARF) is first investigated. Ellipticity is defined as the ratio of the major axis to the minor axis ($e_1 = a/b$). The initial parameters of the Bar-THz HC-ARF are $a = b \times e_1$, $b = 1.05$ mm, $e_1 = 2.6$, $t_1 = 0.3$ mm, $t_2 = 0$ mm, and $d = 3.3$ mm (that is, S-THz HC-ARF). The other structural parameters, $R = 4.65$ mm and $h = 1$ mm, are fixed in the subsequent analysis. Both the mesh elements and PML parameters are optimized to improve the accuracy. The mesh element size is not greater than 0.05 mm in the region of the photosensitive resin and air core, and less than 0.08 mm in the hollow areas of the cladding. The thickness of PML is 2.0 mm with a maximum mesh size of less than 0.2 mm.

Figure 2 shows the simulated loss and the effective refractive indexes of the X- and Y-polarized FMs. The two-loss peaks at 0.37 THz and 0.74 THz in the frequency range from 0.2 to 1.0 THz agree with the theoretical resonant frequencies for $m = 1$ and $m = 2$ as marked by the gray dashed-line calculated by Eq. (1) for $t_1 = 0.3$ mm. This demonstrates that the guidance mechanism stems from the anti-resonant effect in the THz HC-ARF guide. Furthermore, the corresponding

Optics EXPRESS

changes can be observed from the resonant frequencies according to the effective refractive index curves of the two polarized FMs as shown in Fig. 2 (b). Low loss and high birefringence can be obtained at 0.3 THz, as shown in Fig. 2, which provides the theoretical basis for subsequent simulation.

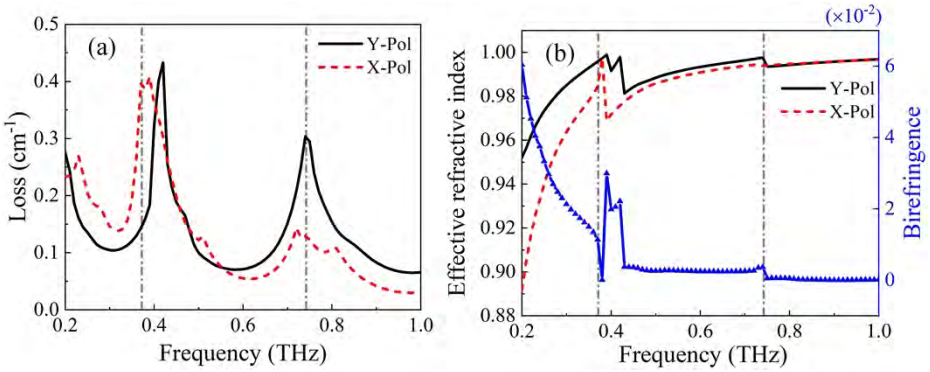

Fig. 2. (a) Loss (b) Effective refractive index and birefringence as functions of frequencies for the S-THz HC-ARF.

Figure 3 shows the mode field distributions of the X- and Y- polarized FMs for different minor axes of elliptical tube b at 0.30 THz and 0.37 THz, respectively. As shown in Fig. 3 (b), for a larger core size (b = 1.7 mm) at the resonant frequency of 0.37 THz, the FMs field spreads into the cladding area whereas the FMs field is confined at 0.30 THz, which is far away from the resonant frequencies. However, with decreasing b (b = 1.05 mm), the Y-polarized FM and X-polarized FM are coupled with cladding mode when the core is relatively small. Figure 3 (a) shows that the core power is transferred to the cladding area at the anti-resonant frequency of 0.30 THz. At 0.37 THz, the FMs field spreads into the cladding area due to resonant coupling consistent with Fig. 3 (b). Therefore, the mode field distribution for a larger core size verifies that the S-THz HC-ARF conforms to the anti-resonant guidance mechanism. The loss and birefringence for different b values at the anti-resonant frequency 0.3 THz are given in Fig. 3. It can be seen that the loss increases with decreasing core size, while the birefringence value increases. In order to achieve higher birefringence, a smaller core is adopted in optimizing the structural parameters.

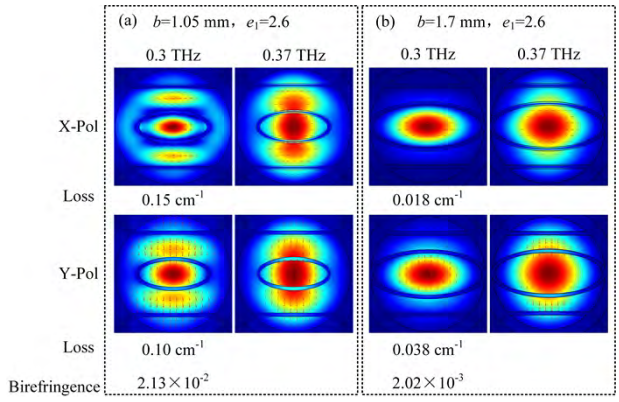

Fig. 3. Mode field distributions and loss of X- and Y-polarized FMs as well as birefringence for different minor axes of the elliptical tube b.

Optics EXPRESS

3. Structural optimization

The structural parameters affect the performance of the S-THz HC-ARF. For the targeted frequency of 0.3 THz, the effects of various parameters including the core size (a and b), spacing of the slabs (d), tube wall thickness (t_1), and supporting bars (t_2) are assessed.

3.1. Core size

As shown in Fig. 1, the core size of the S-THz HC-ARF is determined by the major axis (a) and minor axis (b) of the elliptical tube and plays an important role in the birefringence and loss. Here, $e_1 = a/b$ where e_1 is the tube ellipticity and the other parameters are $t_1 = 0.3$ mm and $d = 3.3$ mm. The simulation results of the birefringence as a function of b for $e_1 = 2.56$, 2.58, 2.6, 2.62, and 2.64 are presented at a fixed frequency of 0.30 THz in Fig. 4 (a). The birefringence curves change abruptly at which the birefringence curve moves in the direction of decreasing b with increasing e_1. To determine the reason for the abrupt change in the birefringence curve, Fig. 5 shows the effective refractive indexes of Y-polarized FM, X-polarized FM, and X-polarized cladding modes at $e_1 = 2.6$ as a function of b at 0.3 THz. The b value range is expanded to 0.9-1.3 mm to better display the effective refractive index change. The shaded area in Fig. 5 is the part in which structural parameter optimization is performed as shown in Fig. 4. There is an abrupt change in the effective refractive index curves of the X-polarized FM and X-polarized cladding mode at the b of 1.06 mm. When $b = 1.06$ mm, the indexes of the two approximate modes (X-polarized FM and X-polarized cladding mode) match and coupling occurs. The avoided crossing occurs and the two true modes become hybrid modes residing both in X-polarized FM and X-polarized cladding mode. When $b > 1.06$ mm, the indexes of the two approximate modes do not match and coupling is inhibited. The fields of the two true modes mainly reside in either the X-polarized FM or X-polarized cladding mode. This can also be observed from the corresponding mode field distributions at $b = 0.9$ mm, 1.06 mm, and 1.2 mm shown in the insets in Fig. 5. On the contrary, there is no abrupt change in the effective refractive index of Y-polarized FM when b changes from 0.9 mm to 1.3 mm. Figure 4 (a) shows that the birefringence is on the order of 10^{-2} before the abrupt point, while it is 10^{-3} after the abrupt point. Furthermore, the birefringence of the S-THz HC-ARF with different e_1 shows a negative correlation function with b before the abrupt point. For example, the birefringence decreases monotonically from 2.26×10^{-2} to 2.12×10^{-2} as b increases from 1.0 to 1.05 mm for e_1 being of 2.6.

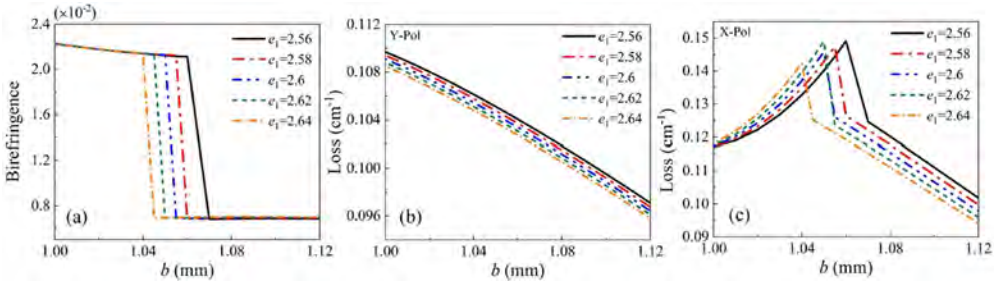

Fig. 4. (a) Birefringence and Loss of (b) Y- and (c) X-polarized FMs of the S-THz HC-ARF for different e_1 as a function of b at 0.3 THz.

Figures 4 (b) and (c) present the simulated losses of Y-and X-polarized FMs as a function of b for e_1= 2.56, 2.58, 2.6, 2.62, and 2.64, respectively. Figure 4 (b) shows that the loss of Y-polarized FM decreases monotonically with increasing b and/or e_1 because the size of the hollow core increases as b and/or e_1, and so relatively low loss is observed from the Y-polarized FM. The loss of Y-polarized FM only varies between 0.096 cm^{-1} and 0.11 cm^{-1} when b changes from 1.0 mm to 1.12 mm and e_1 changes from 2.56 to 2.64. However, Fig. 4 (c) reveals a

Optics EXPRESS

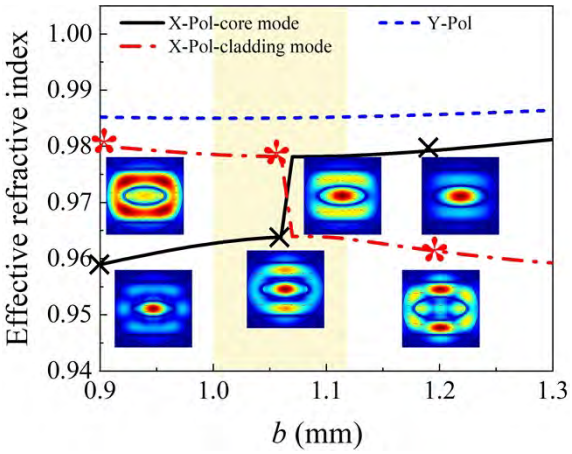

Fig. 5. Effective refractive indexes of Y-polarized FM, X-polarized FM, and X-polarized cladding modes for $e_1 = 2.6$ as a function of b at 0.3 THz.

different trend for the loss of X-polarized FM. When e_1 is fixed, the loss of X-polarized FM increases initially and then decreases. The loss of X-polarized FM varies between 0.094 cm^{-1} and 0.15 cm^{-1} when b changes from 1.0 mm to 1.12 mm and e_1 from 2.56 to 2.64. Based on the above discussion, small b and e_1 give rise to high birefringence but at the expense of high loss. There is thus a trade-off between the birefringence and loss when choosing the suitable d and e_1. Here, b is set to be 1.05 mm and e_1 2.6 to accomplish high birefringence and low loss.

3.2. Slab spacing

Figure 6 shows the birefringence and loss as a function of d at 0.3 THz for the S-THz HC-ARF for $b = 1.05$ mm, $e_1 = 2.6$, and $t_1 = 0.30$ mm. When d changes from 2.8 to 3.8 mm, there is also an abrupt change in the birefringence for d of 3.26 mm because the indexes of the two approximate modes (X- polarized FM and X- polarized cladding mode) match, and coupling occurs when $d = 3.26$ mm. This is confirmed by the effective refractive indexes of Y-polarized FM, X-polarized FM, and X-polarized cladding modes as a function of d at 0.3 THz in Fig. 7. The mode field distributions for $d = 2.8$ mm, 3.3 mm, and 3.8 mm are also shown. Before the abrupt point ($d < 3.26$ mm), the modal birefringence decreases from 8.64×10^{-3} to 7.05×10^{-3}, which has a magnitude of 10^{-3}. After the abrupt point ($d \geq 3.26$ mm), the modal birefringence decreases from 2.17×10^{-2} to 1.85×10^{-2} and has the order of 10^{-2}. The losses for X- and Y-polarized FMs are different when d changes from 2.8 to 3.8 mm. The loss of Y-polarized FM decreases slightly in the beginning and then increases with d. The Y-polarized FM exhibits the lowest loss of 0.10 cm^{-1} when $d = 3.65$ mm, while the loss of X-polarized FM shows a loss peak due to mode coupling when $d = 3.26$ mm. The loss of X- polarized FM increases first and then decreases as d changes from 2.8 mm to 3.26 mm. The loss of X- polarized FM decreases monotonically from 0.16 cm^{-1} to 0.068 cm^{-1} as d increases from 3.26 mm to 3.8 mm. Considering the preparation feasibility and transmission characteristics of THz HC-ARF, d is set to 3.5 mm to prevent slabs from adhering to the outer circular tube in order to attain both high birefringence and low loss at the same time.

3.3. Wall thickness of the supporting bar

The supporting bars t_2 mechanically maintain the connection between the elliptical core and the outer circular tube. The effects of the wall thickness t_2 of the supporting bar on the birefringence and loss of Bar-THz HC-ARF are investigated. As t_2 is varied, the other parameters are fixed at

Optics EXPRESS

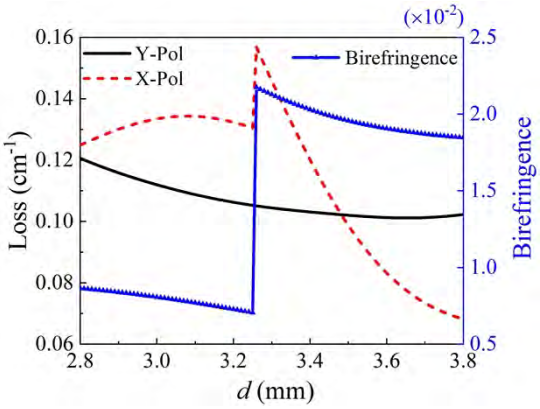

Fig. 6. Birefringence and loss as a function of d at 0.3 THz.

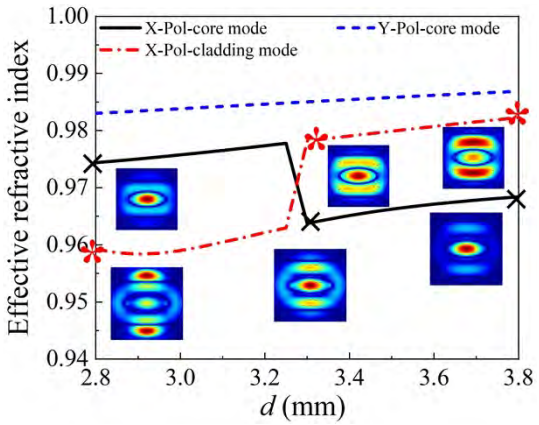

Fig. 7. Effective refractive indexes of Y-polarized FM, X-polarized FM and X-polarized cladding modes as a function of d at 0.3 THz.

$b = 1.05$ mm, $e_1 = 2.6$, $d = 3.5$ mm, and $t_1 = 0.30$ mm. As shown in Fig. 8, the birefringence and loss remain basically unchanged with t_2. The losses of the Y-polarized FM, X-polarized FM, birefringence only vary between 0.104 cm^{-1} and 0.107 cm^{-1}, 0.141 cm^{-1} and 0.142 cm^{-1}, and 2.029×10^{-2} and 2.033×10^{-2} when t_2 is changed from 0.25 mm to 0.45 mm, respectively. As expected, the supporting bars have negligible impact on the birefringence and losses of Bar-THz HC-ARF. The performance of Bar-THz HC-ARF ($t_2 = 0.35$ mm) and S-THz HC-ARF ($t_2 = 0$ mm) are compared as a function of frequencies, and as shown in Fig. 9, the variations of t_2 do not affect the birefringence and losses of the Y-and X-polarized FMs in the frequency range between 0.2 THz and 1.0 THz. Hence, the supporting bar t_2 can be determined according to the actual THz HC-ARF requirements.

3.4. *Wall thickness*

The effects of the wall thickness t_1 of the core and cladding elements on the birefringence and loss are investigated for the Bar-THz HC-ARF with $b = 1.05$ mm, $e_1 = 2.6$, $d = 3.5$ mm, and $t_2 = 3.5$ mm. As shown in Fig. 10, as t_1 increases from 0.25 mm to 0.4 mm with increments of 0.05 mm, the loss peaks shift to lower frequencies consequently shifting the transmission window. The resonant frequencies corresponding to the loss peaks are inversely proportional to

Optics EXPRESS

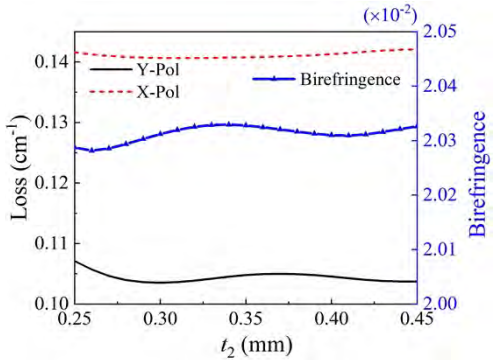

Fig. 8. Birefringence and loss as a function of t_2 at 0.3 THz.

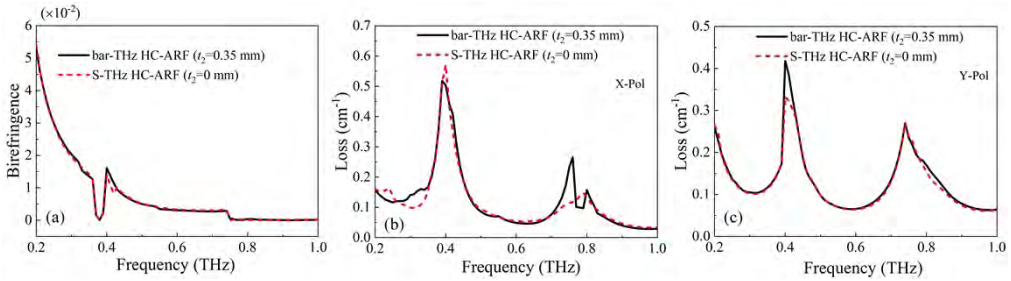

Fig. 9. (a) Birefringence; Loss of (b) X - and (c) Y- polarized FMs of the Bar-THz HC-ARF ($t_2 = 0.35$ mm) and S-THz HC-ARF ($t_2 = 0$ mm) as a function of frequencies.

the wall thickness t_1. The transmission bandwidths with high-birefringence above 1.0×10^{-3} are 0.62, 0.41, 0.29, and 0.37 THz for $t_1 = 0.25$, 0.3, 0.35, and 0.4 mm, respectively. Meanwhile, in the high-birefringence transmission window, the losses of X-and Y-polarized FMs are less than $0.2\,\mathrm{cm}^{-1}$. That is, Bar-THz HC-ARF has an acceptable low-loss window in the high-birefringence regions indicated by the gray regions in Fig. 10. Especially, the transmission bandwidths with high birefringence above 1.0×10^{-2} and the losses less than $0.2\,\mathrm{cm}^{-1}$ are 0.16, 0.14, 0.07, and 0.03 THz for $t_1 = 0.25$, 0.3, 0.35, and 0.4 mm as shown by the black dashed-line and arrows, respectively. With increasing t_1, the transmission bandwidths with high-birefringence above 1.0×10^{-2} shrink. To the best of our knowledge, this is the highest birefringence observed from THz HC-ARFs so far. The numerical results demonstrate that t_1 plays a crucial role in transmission bandwidth with high birefringence and low loss for the Bar-THz HC-ARF. A small wall thickness t_1 offers a wide transmission bandwidth with high birefringence and low loss, but manufacturing is more difficult. As a result, the wall thickness t_1 can be selected according to the actual preparation requirements of THz HC-ARF.

Optics EXPRESS

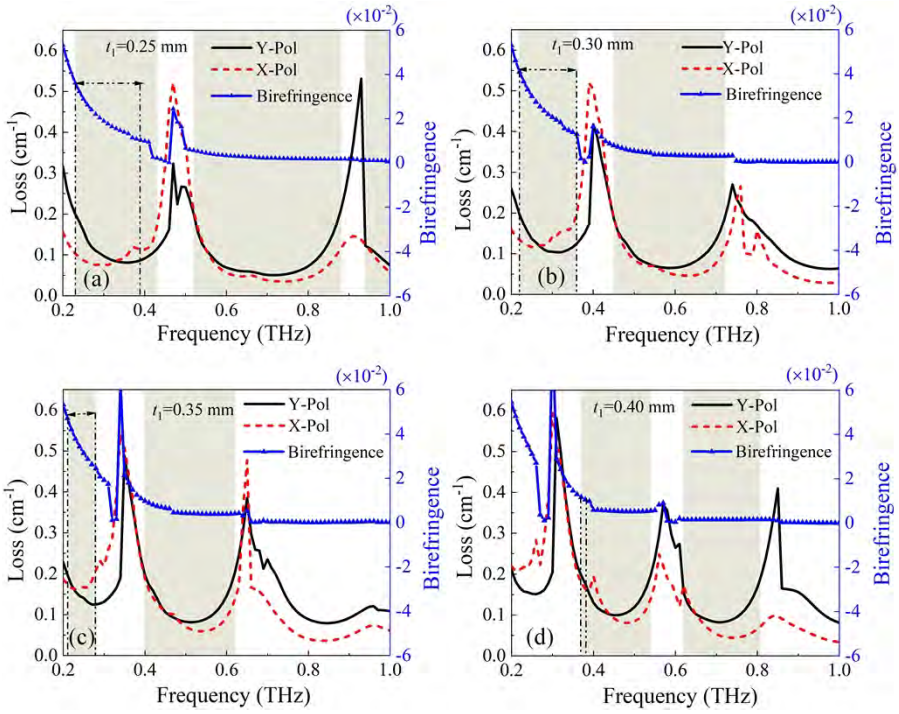

Fig. 10. Birefringence and loss of the Bar-THz HC-ARF with different wall thickness t_1 as a function of frequencies.

4. Experimental results and discussion

4.1. Properties of THz HC-ARF materials

A photosensitive resin is used to manufacture the Bar-THz HC-ARF and the properties of the photosensitive resin and the Bar-THz HC-ARF are determined by THz time domain spectroscopy (THz-TDS) setup as shown in Fig. 11. Pulses from a femtosecond laser at $\lambda \sim 1560$ nm are transmitted through a beam splitter. One part of the fs-laser beam is directed through an optical delay line used to adjust the propagating time of the wave and the other irradiates the THz emitter to generate the THz beam. In the THz-TDS system, the THz sources are in a horizontally polarized state. The time-domain pulse signals with and without the sample are measured and the frequency-domain signals are deduced by Fast Fourier Transformation (FFT) to obtain the time-domain signals. Therefore, both the signal phase φ and the electric field component E as a function of frequencies are resolved.

The photosensitive resin with a thickness of about 1.08 mm and a diameter of 13 mm is printed by a 3D printer. A reference comparison method is used to obtain the complex refractive index ($\tilde{n} = n + ik$) of the sample, where n is the real part corresponding to the effective refractive index and k is the imaginary part related to the attenuation coefficient α of sample. By comparing the signal phase delay $\Delta\varphi$ and intensity reduction with the reference signal, the real part n and the attenuation coefficient α of the sample can be determined as shown below [1]:

$$n = \frac{\Delta\varphi c}{2\pi f L} + 1 \tag{4}$$

$$\alpha = \frac{2\ln(E_{\text{sam}}/E_{\text{ref}})}{L}, \tag{5}$$

Optics EXPRESS

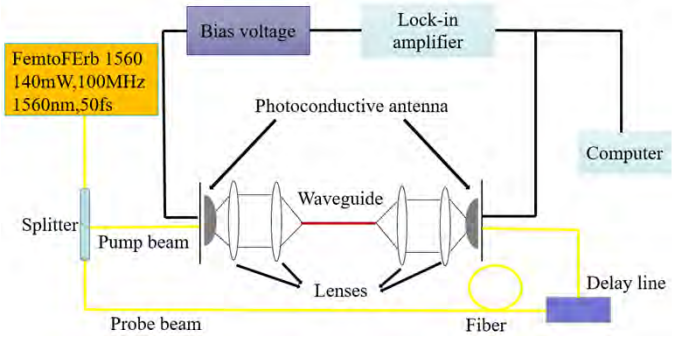

Fig. 11. Schematic diagram of the THz-TDS setup.

where $\Delta\varphi = \varphi_{sam}$-$\varphi_{ref}$ indicates the phase difference between the sample and the reference signal, E_{sam} and E_{ref} are the electric field component of the sample and reference signal, respectively, L is the thickness of the sample, c is the speed of light in vacuum, f is the frequency of THz signal. The imaginary part k refers to the extinction coefficient, which can be calculated in terms of the attenuation coefficient α as follow [1]:

$$k = \frac{\alpha c}{4\pi f} \tag{6}$$

Figure 12 exhibits the calculated n and k of the materials in the frequency range between 0.2 and 1 THz. The refractive index n is measured to be 1.6778 and nearly constant in the entire frequency range. The imaginary part k increases monotonically from 0.027 at 0.2 THz to 0.062 at 1.0 THz. The average refractive index of the photosensitive resin is 1.6778 + i 0.045 in the frequency range from 0.2 to 1.0 THz. The measurement results are used to model the properties of the THz HC-ARF as described in Section 3.

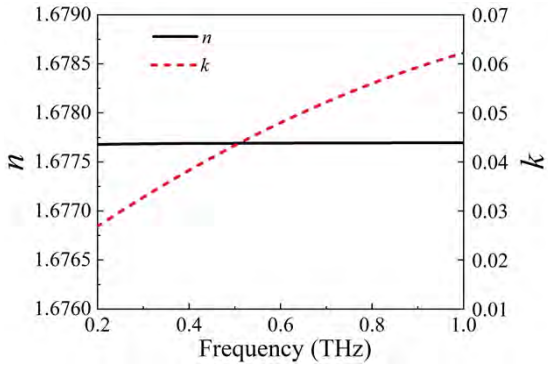

Fig. 12. Real part n and imaginary part k of material as a function of frequencies.

4.2. Characteristics of THz HC-ARF

The cross-sections of the Bar-THz HC-ARFs are depicted in Fig. 13. Owing to the limited accuracy of 3D printing, during the actual preparation of Bar-THz HC-ARF, the slab adheres to the outer circular tube. Therefore, the inner wall of the outer circular tube is engraved with a 0.5 mm thick notch (notch Bar-THz HC-ARF) without changing the characteristics of Bar-THz HC-ARF, and the cross-section is shown in Fig. 13 (b). Two lengths (100 mm and 150 mm) of

Optics EXPRESS

the notch Bar-THz HC-ARF are prepared by the photosensitive resin as shown in Fig. 13 (c). The structural parameters of the Bar -THz HC-ARF samples are set as $a = b \times e_1$, $b = 1.05$ mm, $e_1 = 2.6$, $t_1 = 0.3$ mm, $t_2 = 3.5$ mm, and $d = 3.5$ mm. The wall thickness $t_1 = 0.3$ mm is almost the minimum for the 3D printing fabrication capacity. The fabricated fiber dimensions are in good agreement with the design within the expected tolerance of the 3D printer.

Fig. 13. Cross-sections of (a) standard Bar-THz HC-ARF, (b) notch Bar-THz HC-ARF, (c) Notch Bar-THz HC-ARF fabricated by 3D printing.

The transmission measurements are performed the notch Bar-THz HC-ARF by THz-TDS. Three measurement conditions are adopted here as described previously [1]. In particular, the incident signal should be kept consistent to measure the transmission of the X- and Y-polarized modes through the notch Bar-THz HC-ARF. As shown in the inset in Fig. 15, the X- and Y-polarized modes can be obtained by placing the notch Bar-THz HC-ARF parallel or perpendicular without changing the incident signal. In addition, the transmission loss of the notch Bar-THz HC-ARF samples is determined by the 'cut-back' method. Two different lengths of sample (150 mm and 250 mm) are measured. Since the maximum length is restricted by the working distance of the 3D printer, a 250 mm long sample is fabricated by connecting the 100 mm and 150 mm long samples as shown in Fig. 14.

Fig. 14. Photograph of connected notch Bar-THz HC-ARF.

The THz-TDS detector detects the train of fs-laser pulses from the time delay line and transmitted THz wave from the THz HC-ARF sample. The THz pulse in Fig. 15(a) is the reference signal that passes through a circular aperture with a hole diameter of 6 mm. The experimentally measured pulses after propagating through the notch Bar-THz HC-ARFs with lengths of 150 mm and 250 mm in the X-and Y-polarized directions. Figures 15 (c) and (d) show that when the THz pulse passes through the longer notch Bar-THz HC-ARF (250 mm long) in the X-polarized direction, it arrives at the detector at 895 pico-second (ps) and propagates along the shorter notch Bar-THz HC-ARF (150 mm long) at about 563 ps. Compared to the reference signal (Fig. 15 (a)), we observe a time lag of 513 ps for the 150 mm length and 845 ps for the 250 mm length in the notch Bar-THz HC-ARFs. The time delay introduced between the temporal waveforms of the reference and notch Bar-THz HC-ARF indicates that the pulses travel mainly in the air core of the notch Bar-THz HC-ARF. The dispersion effect can be qualitatively observed from the spreading of the envelope of the temporal waveform of the notch Bar-THz HC-ARFs compared to that of the reference waveform. In addition, as shown in Figs. 15 (b) and (c), the amplitude of the X-polarized FM is higher than that of the Y-polarized FM when the

Optics EXPRESS

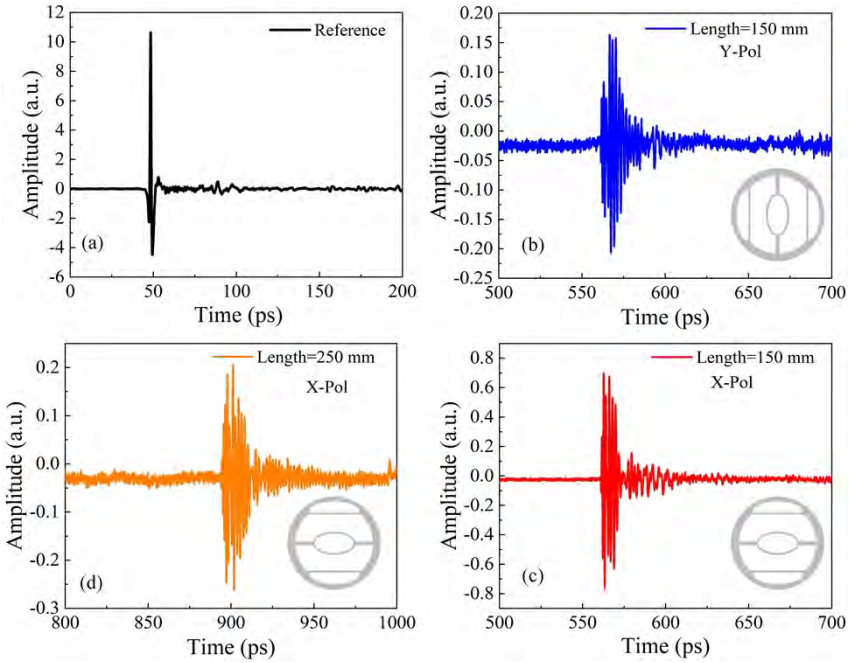

Fig. 15. Measured THz pulses for (a) reference signal and (b) transmitted pulse through a 150-mm-long notch Bar-THz HC-ARF for Y-polarized FM, (c) 150-mm-long notch Bar-THz HC-ARF for X-polarized FM, and (d) 250-mm-long notch Bar-THz HC-ARF for X-polarized FM.

time-domain traces after propagation through the 150 mm long notch Bar-THz HC-ARF, which means that the X-polarized FM has a smaller loss than the Y-polarized FM.

Figure 16 shows the birefringence, losses of X- and Y-polarized FMs determined from the experiments, as well as the simulated results of the notch Bar-THz HC-ARF and Bar-THz HC-ARF. The simulation is carried out using the designed structural parameters to investigate the transmission characteristics of these two types of Bar-THz HC-ARF. Bar-THz HC-ARF shows no significant effects on the simulated birefringence and losses of Y-and X-polarized FMs whether or not there are notches or not over the frequency range from 0.2 THz to 1.0 THz. The variation of birefringence of notch Bar-THz HC-ARF for $t_1 = 0.30$ mm in the frequency range of 0.2 THz to 1 THz is shown in Fig. 16 (a) which discloses that the measured birefringence is within the range of 2.17×10^{-2} to 3.72×10^{-2} in the low-frequency transmission window (0.2 to 0.27 THz), 1.07×10^{-3} to 6.6×10^{-3} in the 0.41 THz -0.51 THz transmission window, and on the order of 10^{-4} to 10^{-5} in the high-frequency transmission window (0.51 to 1.0 THz). The highest birefringence is 3.72×10^{-2} at 0.22 THz, which is lower than the simulated result of 4.61×10^{-2} at 0.21 THz. Moreover, the simulated birefringence is in the range of 1.31×10^{-2} to 4.61×10^{-2} in the low-frequency transmission window (0.21 to 0.35 THz), 2.8×10^{-3} to 7.8×10^{-3} in the 0.45 THz -0.72 THz transmission window, and on the order of 10^{-4} to 10^{-5} in the high-frequency transmission window (0.78 to 1.0 THz). The birefringence difference between experiments and simulation is mainly caused by the slight difference between the sample parameters and design parameters. Nonetheless, the fabricated THz HC-ARF shows the highest birefringence among currently reported THz HC-ARFs.

The experimental and numerical losses of the X-and Y-polarized FMs are shown in Figs. 16 (b) and (c). The experimental and numerical loss spectra of the X- and Y-polarized FMs exhibit a comb-like distribution. The positions of the experimental loss peak red-shift compared to the

Optics EXPRESS

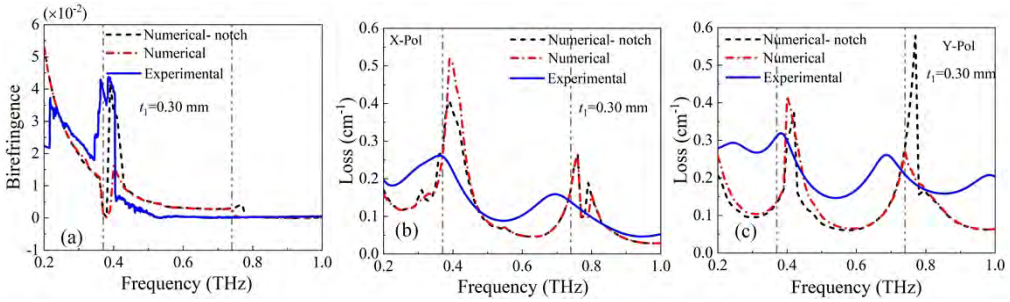

Fig. 16. Comparison of experimental and simulation results: (a) Birefringence and Loss of (b) X- and (c) Y-polarized FMs as a function of frequencies for $t_1 = 0.30$ mm.

numerical results due to the uneven wall thickness of slightly more than 0.3 mm. As shown in Figs. 16 (b) and (c), the discrepancies in the measured and simulated transmission losses can be attributed to the variation in the sample fabrication process. Overall, the experimental data show good agreement with the simulated results. The measured losses of the X- and Y-polarized FMs are in the ranges of 0.18 to 0.20 cm^{-1} and 0.28 to 0.29 cm^{-1} in the transmission window with birefringence of 10^{-2} (0.2 to 0.27 THz), respectively, and 0.09 to 0.20 cm^{-1} and 0.15 to 0.28 cm^{-1} in the transmission window with birefringence of 10^{-3} (0.41 to 0.51 THz), respectively. In addition, the measured highest birefringence is 3.72×10^{-2} at 0.22 THz and the corresponding losses of X- and Y-polarized FMs are 0.18 and 0.29 cm^{-1}, respectively. Similarly, the losses of X-and Y-polarized FMs obtained by numerical analysis are in the ranges of 0.12 to 0.18 cm^{-1} and 0.10 to 0.19 cm^{-1} in the transmission window with birefringence of 10^{-2} (0.21 to 0.35 THz), respectively, and those obtained by numerical analysis are 0.045 to 0.17 cm^{-1} and 0.06 to 0.19 cm^{-1} in the transmission window with birefringence of 10^{-3} (0.45 to 0.72 THz), respectively. The highest simulated birefringence is 4.61×10^{-2} at 0.21 THz and the corresponding losses of X-and Y-polarized FMs are 0.15 and 0.19 cm^{-1}, respectively. The experimental results show that the loss of Y-polarized FM is higher than that of X-polarized FM, which is consistent with numerical results. All in all, high-birefringence, low-loss and wide-bandwidth are achieved at the same time from the THz HC-ARF.

A comparison of the birefringence and transmission losses of our THz HC-ARF with those of recently reported THz HC-ARFs is shown in Table 1. Although the THz HC-ARF in Ref. [24] achieves high birefringence and low loss, it lacks experimental confirmation for the high birefringence characteristics. Among the different THz HC-ARFs, those described in Refs. [1] and [27] have relatively low losses and have been verified experimentally, but their birefringence values have a magnitude order of 10^{-3}. As shown in Fig. 3, the loss decreases with increasing core size, while the birefringence value decreases. There is a trade-off between the birefringence and losses by choosing the suitable b and e_1 values. Our design focuses on achieving high birefringence, and the loss value is relatively high. If a relatively large core diameter is selected, the birefringence is 2.02×10^{-3} at 0.3 THz and the corresponding loss is 0.018 cm^{-1}. Compared with the THz HC-ARFs reported in Refs. [26], [28], and [31–33], our THz HC-ARF with a large core diameter has high birefringence and relatively low loss, which can confine most of the energy in the core. Only a very small amount of energy leaks into the cladding. Therefore, this design can greatly reduce the influence of material absorption on fiber loss. The results show that the core diameter can be varied according to the actual requirements. The birefringence and transmission loss properties of our design indeed show better balances compared with other THz HC-ARFs. More importantly, our THz HC-ARF with a small core diameter has an experimental birefringence on the order of 10^{-2}.

Optics EXPRESS

Table 1. Comparison of the birefringence and transmission loss properties between our THz HC-ARF and recently reported THz HC-ARFs

References	Materials	Operating Frequencies (THz)	Core diameter (mm)	Numerical birefringence	Numerical loss (cm^{-1})	Experimental birefringence	Experimental Loss (cm^{-1})
Ref. [24]	Polymer	1	0.4	0.01	0.02	×	×
Ref. [26]	Topas	1.2	1.885	7.31×10^{-4}	0.005	×	×
Ref. [27]	SomosEvoLVe 128	0.2-0.5	9	10^{-3}	0.005	10^{-4}	0.05-0.1
Ref. [28]	Zeonex	0.9	2.8	1.52×10^{-4}	0.0012	×	×
Ref. [31]	Topas	1.22-1.40	2	10^{-4}	0.02	×	×
Ref. [32]	Zeonex	1.1	1.9	Above 10^{-4}	0.0008	×	×
Ref. [33]	COC	2.5	2	1×10^{-5}	0.0023	×	×
Ref. [1]	Photosensitive resin	0.39-0.50	5	10^{-3}	0.04 - 0.15	10^{-3}	0.05 - 0.12
our work	Photosensitive resin	0.2 - 0.27	2.73	10^{-2}	0.12 - 0.18	2.17×10^{-2} to 3.72×10^{-2}	0.18 - 0.20

5. Conclusion

A THz HC-ARF is designed and the propagation properties including the birefringence and losses are determined theoretically and experimentally. The materials parameters including the extinction coefficient and effective index are investigated to obtain the optimal geometric parameters of the THz HC-ARF. Numerical results predict that the birefringence reaches the level of 10^{-2} and the loss is in the range of 0.12 to 0.18 cm^{-1} in the transmission window between 0.21 and 0.35 THz. The highest simulated birefringence is 4.61×10^{-2} at 0.21 THz and the corresponding loss is 0.15 cm^{-1}. Experimental verification is performed on the 3D-printed THz HC-ARF by THz-TDS. The birefringence variation of the notch Bar-THz HC-ARF is in the range of 2.17×10^{-2} to 3.72×10^{-2} in the 0.2 to 0.27 THz transmission window. The highest birefringence is 3.72×10^{-2} at 0.22 THz and the corresponding loss is 0.18 cm^{-1}. The loss of the notch Bar-THz HC-ARF is 0.18 to 0.20 cm^{-1} in the high-birefringence transmission window (0.2 to 0.27 THz). Our THz HC-ARF thus shows the highest birefringence and relatively low loss in comparison with similar THz HC-ARFs reported recently. Comparing our 3D-printed THz HC-ARFs [1], [22], [27] and those described in Refs. [34–36], the experimental and numerical results are consistent, indicating that the properties of 3D-printed THz HC-ARFs can be predicted and controlled. The results also reveal that 3D printing is an effective technique for the fabrication of THz devices and development of THz technology. Additionally, we believe that with the development of 3D printing technology, there will be more low absorption materials suitable for the production of THz HC-ARF that can be used.

Funding. National Natural Science Foundation of China (12174022); Beijing Municipal Natural Science Foundation (1232028); City University of Hong Kong (9220061, 9229021).

Disclosures. The authors declare that there are no conflicts of interest related to this article.

Data availability. Data underlying the results presented in this paper are not publicly available at this time but may be obtained from the authors upon reasonable request.

References

1. L. Xue, X. Z. Sheng, S. Lou, G. Zhao, S. Yang, Z. Xing, and H. Jia, "High-birefringence low-loss hollow-core THz waveguide embedded parallel slab cladding," Photonics Views **17**(5), 36–39 (2020).
2. M. T. Ali Khan, H. Li, Y. Liu, G. D. Peng, and S. Atakaramians, "Compact terahertz birefringent gratings for dispersion compensation," Opt. Express **30**(6), 8794–8803 (2022).
3. W. Luo, P. Jiang, Q. Xu, L. Cao, A. Jones, K. Li, N. Copner, and Y. Gong, "Terahertz sensor via ultralow-loss dispersion-flattened polymer optical fiber: design and analysis," Materials **14**(17), 4921 (2021).

Optics EXPRESS

4. G. K. M. Hasanuzzaman, S. Rana, and M. S. Habib, "A novel low loss, highly birefringent photonic crystal fiber in THz regime," IEEE Photonics Technol. Lett. **28**(8), 899–902 (2016).
5. E. Reyes-Vera, J. Usuga-Restrepo, C. Jimenez-Durango, J. Montoya-Cardona, and N. Gomez-Cardona, "Design of low-loss and highly birefringent porous-core photonic crystal fiber and its application to terahertz polarization beam splitter," IEEE Photonics J. **10**(4), 1–13 (2018).
6. M. Borovkova, M. Khodzitsky, P. Demchenko, O. Cherkasova, A. Popov, and I. Meglinski, "Terahertz time-domain spectroscopy for non-invasive assessment of water content in biological samples," Biomed. Opt. Express **9**(5), 2266–2276 (2018).
7. X. Zhao, J. Xiang, X. Wu, and Z. Li, "High birefringence, single-polarization, low loss hollow-core anti-resonant fibers," Opt. Express **29**(22), 36273–36286 (2021).
8. Y. F. Hong, S. F. Gao, W. Ding, X. Zhang, A. Q. Jia, Y. L. Sheng, P. Wang, and Y. Y. Wang, "Highly birefringent anti-resonant hollow-core fiber with a bi-thickness fourfold semi-tube structure," Laser Photonics Rev. **16**(5), 2100365 (2022).
9. J. Luo, S. Chen, H. Qu, Z. Su, L. Li, and F. Tian, "Highly birefringent single-mode suspended-core fiber in terahertz regime," J. Lightwave Technol. **36**(16), 3242–3248 (2018).
10. B. Wang, C. Jia, J. Yang, Z. Di, J. Yao, and J. Zhang, "Highly birefringent, low flattened dispersion photonic crystal fiber in the terahertz region," IEEE Photonics J. **13**(2), 1–10 (2021).
11. T. Yang, C. Ding, R. W. Ziolkowski, and Y. J. Guo, "A scalable THz photonic crystal fiber with partially-slotted core that exhibits improved birefringence and reduced loss," J. Lightwave Technol. **36**(16), 3408–3417 (2018).
12. M. S. Islam, J. Sultana, A. Dinovitser, B. W. H. Ng, and D. Abbott, "A novel Zeonex based oligoporous-core photonic crystal fiber for polarization preserving terahertz applications," Opt. Commun. **413**, 242–248 (2018).
13. M. Faisal and M. Shariful Islam, "Extremely high birefringent terahertz fiber using a suspended elliptic core with slotted airholes," Appl. Opt. **57**(13), 3340–3347 (2018).
14. Y. Zhang, L. Xue, D. Qiao, and Z. Guang, "Porous photonic-crystal fiber with near-zero ultra-flattened dispersion and high birefringence for polarization-maintaining terahertz transmission," Optik **207**(163817), 163817 (2020).
15. R. Islam, M. S. Habib, G. K. Hasanuzzaman, S. Rana, and M. A. Sadath, "Novel porous fiber based on dual-asymmetry for low-loss polarization maintaining THz wave guidance," Opt. Lett. **41**(3), 440–443 (2016).
16. J. Zhang, J. Cao, B. Yang, X. Liu, Y. Cheng, C. Bao, S. Xie, L. Dong, and Q. Hao, "Ultralow loss hollow-core negative curvature fibers with nested elliptical antiresonance tubes," Opt. Express **30**(10), 17437–17450 (2022).
17. M. S. Habib, A. I. Adamu, C. Markos, and R. Amezcua-Correa, "Enhanced birefringence in conventional and hybrid anti-resonant hollow-core fibers," Opt. Express **29**(8), 12516–12530 (2021).
18. M. S. Islam, C. M. B. Cordeiro, M. A. R. Franco, J. Sultana, A. L. S. Cruz, and D. Abbott, "Terahertz optical fibers [Invited]," Opt. Express **28**(11), 16089–16117 (2020).
19. H. Xiao, H. Li, G. Ren, Y. Dong, S. Xiao, and S. Jian, "Polarization-maintaining hollow-core photonic bandgap few-mode fiber in terahertz regime," IEEE Photonics Technol. Lett. **30**(2), 185–188 (2018).
20. G. Ren, Y. Gong, P. Shum, X. Yu, and J. Hu, "Polarization maintaining air-core bandgap fibers for terahertz wave guiding," IEEE J. Quantum Electron. **45**(5), 506–513 (2009).
21. H. Xiao, H. Li, B. Wu, and S. Jian, "Polarization-maintaining terahertz bandgap fiber with a quasi-elliptical hollow-core," Opt. Laser Technol. **105**, 276–280 (2018).
22. S. Yang, X. Sheng, G. Zhao, S. Lou, and J. Guo, "3D printed effective single-mode terahertz antiresonant hollow core fiber," IEEE Access **9**, 29599–29608 (2021).
23. C. H. Lai, Y. S. Yeh, C. A. Yeh, and Y. K. Wang, "Effective bandwidth of terahertz antiresonant reflecting pipe waveguide," Opt. Express **26**(5), 6456–6465 (2018).
24. D. Chen and H. Chen, "Highly birefringent low-loss terahertz waveguide: Elliptical polymer tube," J. Electromagnet. Wave **24**(11-12), 1553–1562 (2010).
25. L. Vincetti and V. Setti, "Elliptical hollow core tube lattice fibers for terahertz applications," Opt. Fiber Technol. **19**(1), 31–34 (2013).
26. S. Yan, S. Lou, X. Wang, T. Zhao, and W. Zhang, "High-birefringence hollow-core anti-resonant THz fiber," Opt. Quantum Electron. **50**(3), 162 (2018).
27. S. Yang, X. Sheng, G. Zhao, and S. Li, "Simple birefringent Terahertz fiber based on elliptical hollow core," Opt. Fiber Technol. **53**, 102064 (2019).
28. H. Xiao, H. Li, B. Wu, Y. Dong, S. Xiao, and S. Jian, "Low-loss polarization-maintaining hollow-core anti-resonant terahertz fiber," J. Opt. **21**(8), 085708 (2019).
29. Z. Du, Y. Zhou, S. Luo, Y. Zhang, J. Shao, Z. Guan, H. Yang, and D. Chen, "Highly birefringent hollow-core anti-resonant terahertz fiber with a thin strut microstructure," Opt. Express **30**(3), 3783–3792 (2022).
30. J. Sultana, M. S. Islam, C. M. B. Cordeiro, M. S. Habib, A. Dinovitser, M. Kaushik, B. W. H. Ng, H. Ebendorff-Heidepriem, and D. Abbott, "Hollow core inhibited coupled antiresonant terahertz fiber: a numerical and experimental study," IEEE Trans. THz Sci. Technol. **11**(3), 245–260 (2021).
31. I. M. Ankan, M. A. Mollah, A. K. Paul, and K. Chakrabarti, "Polarization-maintaining and polarization-filtering negative curvature hollow core fiber in THz regime," in *2020 IEEE Region 10 Symposium (TENSYMP)*, 612–615 (2020).
32. M. A. Mollah, S. Rana, and H. Subbaraman, "Polarization filter realization using low-loss hollow-core anti-resonant fiber in THz regime," Results Phys. **17**, 103092 (2020).

Optics EXPRESS

33. S. Sun, W. Shi, Q. Sheng, Z. Yan, S. Zhang, J. Zhang, C. Shi, G. Zhang, and J. Yao, "Polarization-maintaining terahertz anti-resonant fibers based on mode couplings between core and cladding," Results Phys. **25**, 104309 (2021).
34. Y. Luo, J. Canning, J. Zhang, and G. D. Peng, "Toward optical fibre fabrication using 3D printing technology," Opt. Fiber Technol. **58**(102299), 102299 (2020).
35. A. L. S. Cruz, C. M. B. Cordeiro, and M. A. R. Franco, "3D Printed Hollow-Core Terahertz Fibers," Fibers **6**(3), 43 (2018).
36. J. Yang, J. Y. Zhao, C. Gong, H. L. Tian, L. Sun, P. Chen, L. Lin, and W. W. Liu, "3D printed low-loss THz waveguide based on Kagome photonic crystal structure," Opt. Express **24**(20), 22454–22460 (2016).